

Title	Determination of specific ion positions of Cr^{3+} and O^{2-} in Cr_2O_3 thin films and their relationship to exchange anisotropy at $\text{Co}/\text{Cr}_2\text{O}_3$ interfaces
Author(s)	Shiratsuchi, Yu; Nakano, Yuuta; Inami, Nobuhito et al.
Citation	Journal of Applied Physics. 2018, 123(10), p. 103903
Version Type	VoR
URL	https://hdl.handle.net/11094/89972
rights	This article may be downloaded for personal use only. Any other use requires prior permission of the author and AIP Publishing. This article appeared in Yu Shiratsuchi, Yuuta Nakano, Nobuhito Inami, Tetsuro Ueno, Kanta Ono, Reiji Kumai, Ryoko Sagayama, and Ryoichi Nakatani, Journal of Applied Physics 123, 103903 (2018) and may be found at https://doi.org/10.1063/1.5020620 .
Note	

The University of Osaka Institutional Knowledge Archive : OUKA

<https://ir.library.osaka-u.ac.jp/>

The University of Osaka

Determination of specific ion positions of Cr^{3+} and O^{2-} in Cr_2O_3 thin films and their relationship to exchange anisotropy at Co/ Cr_2O_3 interfaces

Cite as: J. Appl. Phys. **123**, 103903 (2018); <https://doi.org/10.1063/1.5020620>

Submitted: 25 December 2017 • Accepted: 26 February 2018 • Published Online: 14 March 2018

Yu Shiratsuchi, Yuuta Nakano, Nobuhito Inami, et al.



View Online



Export Citation



CrossMark

ARTICLES YOU MAY BE INTERESTED IN

[Resistive detection of the Néel temperature of \$\text{Cr}_2\text{O}_3\$ thin films](#)

Applied Physics Letters **114**, 022402 (2019); <https://doi.org/10.1063/1.5082220>

[Energy condition of isothermal magnetoelectric switching of perpendicular exchange bias in Pt/Co/Au/ \$\text{Cr}_2\text{O}_3\$ /Pt stacked film](#)

Journal of Applied Physics **124**, 233902 (2018); <https://doi.org/10.1063/1.5047563>

[Magnetoelectric switching of perpendicular exchange bias in Pt/Co/ \$\alpha\$ - \$\text{Cr}_2\text{O}_3\$ /Pt stacked films](#)

Applied Physics Letters **106**, 162404 (2015); <https://doi.org/10.1063/1.4918940>

Journal of Applied Physics **Special Topics** Open for Submissions

Learn More

Determination of specific ion positions of Cr^{3+} and O^{2-} in Cr_2O_3 thin films and their relationship to exchange anisotropy at $\text{Co}/\text{Cr}_2\text{O}_3$ interfaces

Yu Shiratsuchi,^{1,a)} Yuuta Nakano,¹ Nobuhito Inami,^{2,3} Tetsuro Ueno,^{2,4} Kanta Ono,² Reiji Kumai,² Ryoko Sagayama,² and Ryoichi Nakatani¹

¹Department of Materials Science and Engineering, Graduate School of Engineering, Osaka University, Osaka 5650871, Japan

²Institute of Materials Structure Science, High Energy Accelerator Research Organization, Tsukuba 3050801, Japan

³Synchrotron Radiation Research Center, Nagoya University, Furo-cho, Chikusa, Nagoya 4648601, Japan

⁴National Institutes for Quantum and Radiological Science and Technology, Sayo 6795148, Japan

(Received 25 December 2017; accepted 26 February 2018; published online 14 March 2018)

The structures of antiferromagnetic $\text{Cr}_2\text{O}_3(0001)$ thin films with perpendicular exchange bias were investigated using reflection high-energy electron diffraction, X-ray reflectivity, and synchrotron X-ray diffraction. We mainly investigated the specific ion positions of Cr^{3+} and O^{2-} in the corundum structure and discussed their relationship to the magnetic anisotropy of Cr_2O_3 . The $\text{Cr}_2\text{O}_3(0001)$ thin film grown on a $\text{Pt}(111)$ buffer layer exhibited a perpendicular exchange anisotropy density of 0.42 mJ/m^2 , in which the Cr^{3+} position is the primary factor in the enhancement of magnetic anisotropy due to dipolar-interaction. In contrast, the single-crystalline $\text{Cr}_2\text{O}_3(0001)$ film grown on a $\alpha\text{-Al}_2\text{O}_3(0001)$ substrate featured a low exchange magnetic anisotropy of 0.098 mJ/m^2 . In this film, the Cr^{3+} position parameter is an insignificant factor, leading to low magnetic anisotropy. The O^{2-} ion position also differs between the two types of films, which can affect both the magnetic anisotropy energy originating from fine structures and the magneto-electric properties of Cr_2O_3 . *Published by AIP Publishing.*

<https://doi.org/10.1063/1.5020620>

I. INTRODUCTION

Exchange anisotropy is an interface magnetic anisotropy that occurs at a ferromagnetic (FM)/antiferromagnetic (AFM) interface.¹ Exchange anisotropy manifests itself as an exchange bias, a shift of the magnetization curve along a magnetic field axis when the magnetic anisotropy energy density of the AFM layer exceeds the interfacial exchange coupling energy density.^{2–4} As the magnetization curve shifts along a magnetic field axis, the exchange bias field, H_{EX} , becomes higher than the coercivity, H_{C} , and the magnetization of the FM layer is fixed at a certain direction in the zero magnetic field. This unidirectional feature has already been utilized in spin-valve films⁵ and magnetic-tunnel junctions.⁶ In order to ensure this behavior, high H_{EX} and low H_{C} must be achieved simultaneously.^{1,2,7–10} In particular, modern spintronic devices are so designed that the magnetization or spin is directed perpendicular to the film for low-power operation and high integration; the direction of the exchange bias should also be perpendicular to the film. However, the perpendicular exchange bias tends to be lower than the conventional in-plane exchange bias,⁹ and the enhancement of perpendicular exchange bias is still under debate.^{7–11} Recent progress in spintronics enable us to control the exchange bias polarity by a suitable external field such as a magnetic field¹² and an electric field.^{13–20} Such dynamic controllability generates a window of exchange bias, where high perpendicular H_{EX} becomes achievable.

Since the discovery of exchange bias in the 1950s,¹ many efforts have been made to elucidate the microscopic origin of exchange bias.^{2–4,21–25} In spite of these efforts, there is insufficient quantitative understanding of H_{EX} and the exchange anisotropy energy density, J_{K} . The divergent understanding arises from the difficulty in estimating the magnetic anisotropy energy density of the AFM layer, K_{AFM} . On the other hand, various models for the exchange magnetic anisotropy^{21–25} suggest that J_{K} depends on K_{AFM} . In addition, the relationship between K_{AFM} and the structural parameters of the films is often ignored.

Cr_2O_3 is an antiferromagnet that possesses unidirectional magnetic anisotropy and a simple spin alignment. The K_{AFM} of Cr_2O_3 consists of the dipolar contribution between Cr^{3+} spins, K_{dip} , and the fine-structure contribution, K_{FS} , of the individual Cr^{3+} ions arising from higher-order spin-orbit effects.²⁶ The K_{dip} also depends on the crystal structure of the Cr_2O_3 layer, i.e., the lattice parameter and specific ion position of Cr^{3+} ions,²⁷ and thus, it can be determined through detailed structural analysis. We previously reported that a high perpendicular J_{K} ($>0.4 \text{ mJ/cm}^2$) was achieved in $\text{Pt}/\text{Co}/\text{Cr}_2\text{O}_3/\text{Pt}$ stacked films²⁸ and briefly reported that J_{K} depends on the crystalline quality of the Cr_2O_3 layer.²⁹ In our previous report, the soft X-ray magnetic circular dichroism (XMCD) measurements clarified that the amount of interfacial uncompensated AFM Cr spin, i.e., the XMCD intensity, was almost the same for the films with different J_{K} values, in contrast to the Fe-Co/bcc-Mn-Ir film, where J_{K} is proportional to the XMCD intensity of the interfacial uncompensated AFM Mn spins.³⁰ This is probably because of the difference in the origin of the interfacial uncompensated AFM moments. In the case of the FM/Mn-Ir

^{a)}Author to whom correspondence should be addressed: shiratsuchi@mat.eng.osaka-u.ac.jp

system, the interfacial uncompensated moment originated from spin canting from the original direction because of interfacial exchange coupling.^{31,32} In contrast, in the case of the FM/Cr₂O₃(0001) system, the broken degeneracy of the oppositely directed magnetic domain of the boundary magnetization induced the uncompensated interfacial AFM moment.^{29,33} In the latter case, when the Cr₂O₃ layer becomes a single domain, the amount of uncompensated interfacial AFM moments reaches a ceiling. In other words, the above results of XMCD measurements indicate that we need to determine another mechanism for the highly different J_K . In this study, we analyzed the crystal structure of Cr₂O₃ layers grown on different underlayers, namely Pt/Co/Cr₂O₃/Pt/ α -Al₂O₃(0001)-subs. and Pt/Co/Cr₂O₃/ α -Al₂O₃(0001)-subs., yielding different J_K values. In addition, we discuss K_{dip} and K_{FS} using the estimated lattice parameters and specific ion positions.

II. EXPERIMENTAL PROCEDURE

Samples were fabricated using a DC magnetron sputtering system with a base pressure of $<5 \times 10^{-6}$ Pa. The stacking structures of the fabricated films were Pt(1.2)/Co(0.5)/Cr₂O₃(70)/Pt(0, 20)/ α -Al₂O₃(0001)-subs. Two types of films were fabricated, with and without the buffer layer. The Pt buffer layer with a thickness of 20 nm was deposited on an ultrasonically cleaned α -Al₂O₃(0001) substrate at 873 K, which gave rise to the twinned Pt(111) layer. The Cr₂O₃ layer was deposited on the Pt(111) buffer layer or on the α -Al₂O₃(0001) substrate at 773 K using a reactive sputtering technique with a Ar + O₂ gas mixture. Subsequently, 0.5-nm-thick Co and 1.2-nm-thick Pt capping layers were deposited on the Cr₂O₃ layer at room temperature. The gas pressure during sputtering was 0.5 Pa for Pt and Cr₂O₃ and 0.6 Pa for Co.

The fabricated films exhibited both perpendicular magnetic anisotropy and perpendicular exchange bias. In Fig. 1, the temperature dependence of J_K is shown for both the films. J_K was calculated from $J_K = H_{\text{EX}} \cdot M_S \cdot t_{\text{FM}}$, where M_S and t_{FM} represent the saturation magnetization and the FM layer

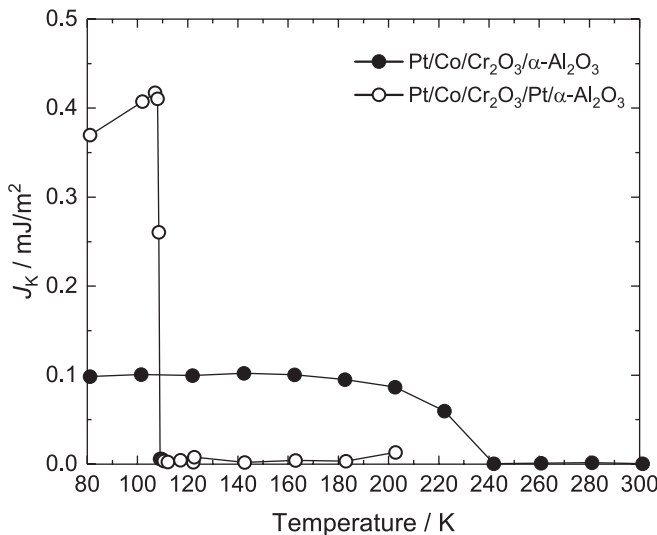


FIG. 1. Temperature dependence of exchange anisotropy energy density (J_K) of Pt/Co/Cr₂O₃/ α -Al₂O₃-subs. (closed circle) and Pt/Co/Cr₂O₃/Pt/ α -Al₂O₃-subs. (open circle).

thickness, respectively. In this work, H_{EX} was measured by magneto-optic Kerr effect (MOKE) magnetometry in the polar configuration as a function of temperature and $M_S \cdot t_{\text{FM}}$, and the saturation magnetization per unit area was measured by vibrating sample magnetometry at room temperature. Note that although the magnetic moment is induced in the Pt capping layer by exchange coupling with Co,^{11,34} as long as the induced moment in Pt is coupled with the Co spin and reversed together with the Co spin, it does not affect the estimation of J_K by considering $M_S \cdot t_{\text{FM}}$. It should also be noted that the Curie temperature, T_C , of the FM layer in our film is above 380 K according to the temperature dependence of the Kerr rotation (not shown), and thus, the reduction of T_C that can occur in the ultrathin film does not affect the estimation of J_K . The film with the Pt buffer layer exhibits a J_K of 0.42 mJ/m², and the exchange bias abruptly vanishes above 109 K. In contrast to the high J_K of the film on the Pt buffer layer, the J_K of the film directly grown on the α -Al₂O₃ substrate is below 0.098 mJ/m², which is less than a quarter of the former J_K . The abrupt disappearance of J_K for the film with the Pt buffer layer and the difference in the blocking temperatures of the two films are quantitatively explained by the energy competition between the interfacial exchange coupling and magnetic anisotropy energy density of the AFM layer per unit area. In this scenario, the gradual decrease in J_K at 200–240 K for the film on the α -Al₂O₃ substrate may be due to the dispersion of J_K and/or K_{AFM} . The details of the temperature dependence of J_K for this system are discussed in our previous reports.^{10,18,35}

In order to determine the origin of the different J_K values in these two film types, we carried out various structural analyses such as reflection high-energy electron diffraction (RHEED), X-ray reflectivity (XRR), and synchrotron X-ray diffraction (XRD). RHEED observations were carried out for the surface of each layer in the chamber directly connected to the deposition chamber. XRR measurements were carried out to estimate the interface roughness of the FM/AFM interface using Cu K_α radiation as the source of incident X-ray. The interface roughness was obtained by fitting the experimental results with the theoretical calculation. The XRR was calculated by the following recurrence formula:

$$\begin{aligned}
 \frac{I}{I_0} &= |R_{n,n+1}|^2 \\
 R_{j,j+1} &= \frac{R_{j-1,j} + F_{j,j+1}}{R_{j-1,j} F_{j,j+1} + 1} a_{j+1}^4 \\
 F_{j,j+1} &= \frac{g_{j+1} - g_j}{g_{j+1} + g_j} \exp \left(-\frac{8\pi^2 g_j g_{j+1} \sigma_j^2}{\lambda^3} \right) \\
 a_{j+1} &= \exp \left(-i \frac{\pi g_{j+1} d_{j+1}}{\lambda} \right) \\
 g_j &= \sqrt{n_i^{*2} - \cos^2 \theta}.
 \end{aligned} \tag{1}$$

Here, I_0 and I are the intensities of the incident and reflected X-rays, θ is an incident angle of X-ray, λ is the wavelength of X-ray, and n_i^* , σ_i , and d_i are the refractive index, interface

roughness, and thickness of each layer. j denotes the layer number from the substrate side; for example, in the case of the Pt/Co/Cr₂O₃/α-Al₂O₃ film, $j=0$ for the α-Al₂O₃ substrate, $j=1$ for the Cr₂O₃ layer, $j=2$ for the Co layer, and $j=3$ for the Pt layer. In n_i^* , the density, atomic number, composition, and atomic scattering factors are included. The atomic scattering factors used were the reported values.^{36,37} For the calculation, the thickness, roughness, and density of each layer were varied as the fitting parameters, whereas the composition of the Cr-O layer was fixed at Cr:O=2:3, i.e., Cr₂O₃. In addition, we assumed that the substrate was infinitely thick and the reflection from the backside of the substrate was negligible. The details of the XRR theory can be found in a previous paper³⁸ and in a textbook.³⁹ The actual fitting was done by using the GlobalFit software of RIGAKU Corp.

The lattice parameters and the specific ion positions of Cr³⁺ and O²⁻ were determined using synchrotron XRD measurements carried out at BL-8B and BL-4C beamlines at the Photon Factory of KEK. At the former beamline, two-dimensional diffraction mappings were obtained using a cylindrical imaging plate for the determination of lattice parameters and Cr³⁺ ion position. The incident X-ray is a linearly polarized light along the horizontal direction, and the wavelength of the incident X-ray was calibrated using the diffraction peaks from CeO₂ powder and the calibrated camera length. The diffraction index and integrated intensity were analyzed by using RAPID AUTO. The latter beamline was used to determine the O²⁻ ion position using one-dimensional $2\theta/\omega$ profiles. All structural characterizations were performed at room temperature.

III. RESULTS AND DISCUSSION

Figure 2 shows the RHEED patterns of the Cr₂O₃ layer grown on the α-Al₂O₃(0001) substrate and the Pt(111) buffer layer. The RHEED patterns of both the films depend on the electron azimuth, i.e., [1100] and [1120] of the substrate. For the former film, the RHEED pattern with the [1100] azimuth is symmetric and that with the [1120] azimuth is asymmetric with respect to the (00) streak. The observed diffraction pattern can be explained by the presence of corundum (0001),⁴⁰ and the asymmetric RHEED pattern for the [1120] azimuth

indicates that the fabricated film is single crystalline. For the Cr₂O₃ layer grown on the Pt(111) buffer layer, while the RHEED pattern with the [1100] azimuth is similar to that shown in Fig. 2(a), that with the [1120] azimuth is also symmetric. The symmetric RHEED pattern is due to the twinned domains with the twin boundary along the [1120] direction. Namely, the two RHEED patterns from the different twin domains are superimposed. The XRR profiles of the two types of films shown in Fig. 3 show clear oscillations up to $2\theta/\omega \sim 8^\circ$, suggesting a sharp interface. The theoretical fittings give rise to the Co/Cr₂O₃ interface roughness of 0.28 nm and 0.25 nm for the films grown on the α-Al₂O₃ substrate and Pt buffer layer, respectively. The interface roughnesses of the two films are very similar, and it is difficult to explain the large difference in J_K from the viewpoint of interface roughness. One may wonder at the different profile shapes of the two types of films despite their similar interface roughnesses. This is because the X-ray reflectivity is insensitive to the interface of the two layers, whose densities are similar. In our case, at the Cr₂O₃/α-Al₂O₃ interface, the densities of the two layers are similar: 5.21 g/cc for Cr₂O₃ and 3.98 g/cc for α-Al₂O₃. Thus, the interference from this layer is weak, and consequently, the oscillation from the Cr₂O₃ layer becomes weak. On the other hand, for the film on the Pt buffer layer, owing to the high density of Pt (21.37 g/cc), the density difference at the Cr₂O₃/Pt interface is larger, and thus, a clear oscillation is observed. The results of crystalline quality, J_K , and the Co/Cr₂O₃ interface roughness are summarized in Table I.

In order to investigate the reason for the difference in J_K , we determined the specific ion positions of Cr³⁺ and O²⁻, both of which affect the K_{AFM} of the Cr₂O₃ layer. Figure 4 shows the typical two-dimensional diffraction patterns of the two types of films. The incidence angle of the X-ray was in the range of 10° – 15° , where 0° denotes the direction parallel to the surface plane. Note that the different diffraction patterns of the two films arise from the different X-ray incidence directions with respect to the crystallographic orientation of the α-Al₂O₃ substrate. The diffraction peaks could be indexed to that of the corundum structure for both the films. Hereafter, the Miller indices using the three axes are used in order to simplify the analysis. Diffractions

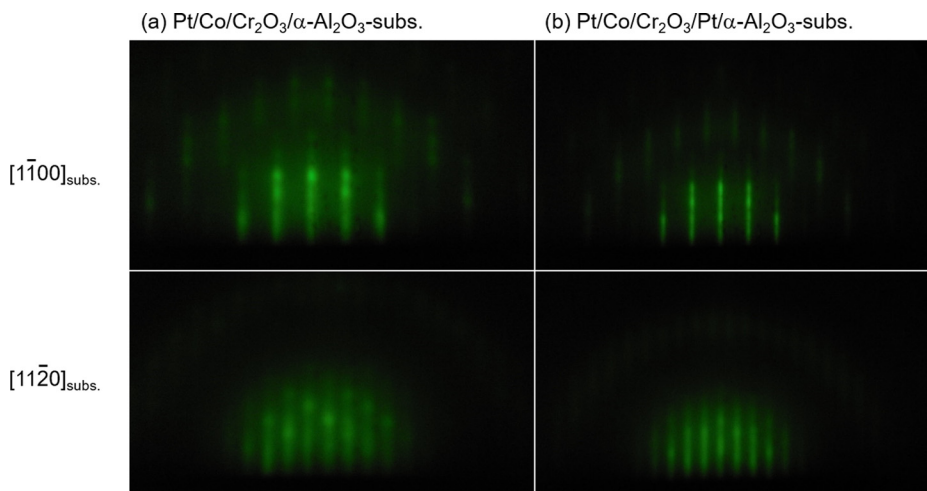


FIG. 2. RHEED patterns of the Cr₂O₃ layer grown on (a) α-Al₂O₃(0001)-subs. and (b) Pt(111) buffer layer. The top and bottom images represent data for the electron azimuth of [1100] and [1120] of the α-Al₂O₃ substrate, respectively.

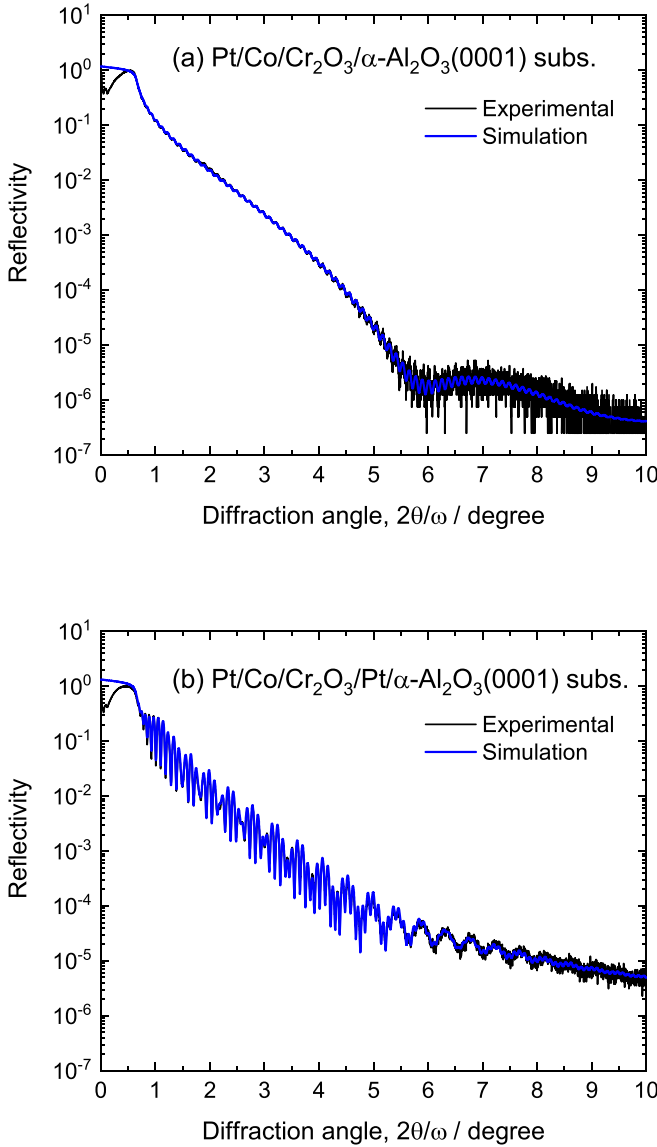


FIG. 3. X-ray reflectivity spectra of (a) Pt/Co/Cr₂O₃/α-Al₂O₃-subs. and (b) Pt/Co/Cr₂O₃/Pt/α-Al₂O₃-subs. The black and blue lines represent the experimental and simulated curves, respectively.

from the Cr₂O₃ layer are observed near the diffraction spot arising from the α-Al₂O₃ substrate, which indicate epitaxial growth [see the arrows in Figs. 4(a) and 4(b)]. For the two films, the lattice parameters a and c estimated from the diffraction patterns are given in Table I. The lattice parameters are not perfectly identical to those of bulk Cr₂O₃, $a = 4.9607 \text{ \AA}$ and $c = 13.599 \text{ \AA}$,⁴¹ possibly because of the epitaxial growth. As indicated by the arrows in Fig. 4(b), although some diffractions namely (0 2 16), (1 2 14), (2 1 10), (1 0 4), (3 1 4), and (1 2 10) are asymmetric for the

substrate because of three-fold symmetry with respect to the (001) pole, these diffractions from the Cr₂O₃ layer are symmetric because of the twinned structure. The diffractions from the different twin domains were labeled as domain 1 and domain 2, which are denoted as the [100] direction of each domain that are parallel or antiparallel to the α-Al₂O₃ substrate, respectively.

We analyzed the integrated diffraction intensity for some diffraction peaks and estimated the specific ion positions by comparing the experimental and simulated diffraction intensities. Figure 5 shows a schematic of the (110) projection-view and the layer-resolved corundum structure. The atomic positions of Cr³⁺ and O²⁻ in the corundum structure are expressed as

$$\left(0, 0, 0; \frac{1}{3}, \frac{2}{3}, \frac{2}{3}; \frac{2}{3}, \frac{1}{3}, \frac{1}{3}\right) + \left(0, 0, \frac{1}{4} + w; 0, 0, \frac{1}{4} - w; 0, 0, \frac{3}{4} + w; 0, 0, \frac{3}{4} - w\right) \text{ for Cr}^{3+}$$

and

$$\left(0, 0, 0; \frac{1}{3}, \frac{2}{3}, \frac{2}{3}; \frac{2}{3}, \frac{1}{3}, \frac{1}{3}\right) + \left(v, 0, \frac{1}{4}; 0, v, \frac{1}{4}; \bar{v}, \bar{v}, \frac{1}{4}; \bar{v}, 0, \frac{3}{4}; 0, \bar{v}, \frac{3}{4}; v, v, \frac{3}{4}\right) \text{ for O}^{2-},$$

where w and v are the specific ion position parameters for Cr³⁺ and O²⁻, respectively, and the values for the bulk Cr₂O₃ are $w = 0.0975$ and $v = 0.3060$ [40]. The Cr³⁺ and O²⁻ coordinates correspond to 12c and 18e sites in Wyckoff positions of group No. 167, $R\bar{3}c$, respectively. w reflects the z-position distance of Cr³⁺ ions from the O²⁻ lattice, and v reflects the asymmetry of the O²⁻ sub-lattice (see Fig. 5). The structural parameter for the $(h \ k \ l)$ diffraction, F_{hkl} , is expressed as follows:

$$F_{hkl}(v, w) = 2 \left\{ 1 + 2 \cos \left(\frac{2}{3} \pi (2h + k + l) \right) \right\} \times \left[f_{\text{Cr}^{3+}} \left\{ 1 + (-1)^l \right\} \cos \left(2\pi \left(\frac{1}{4} + w \right) l \right) + f_{\text{O}^{2-}} \left\{ \cos \left(2\pi \left(vh + \frac{l}{4} \right) \right) + \cos \left(2\pi \left(vk + \frac{l}{4} \right) \right) + \cos \left(2\pi \left(vh + vk - \frac{l}{4} \right) \right) \right\} \right]. \quad (2)$$

Here, $f_{\text{Cr}^{3+}}$ and $f_{\text{O}^{2-}}$ are the atomic scattering factors of Cr⁴² and O,⁴³ respectively. The experimentally obtained

TABLE I. Structural and magnetic parameters of the studied films.

Underlayer/substrate	Crystalline quality	J_K (mJ/m ²)	Co/Cr ₂ O ₃ roughness (nm)	Lattice parameters (Å)		Specific ion position		K_{dip} (104 J/m ³)
				a	c	w	v	
α-Al ₂ O ₃ (0001) subs.	Single crystal	0.098	0.28	4.952	13.600	0.0963	0.332	0.030
Pt(111) buffer layer /α-Al ₂ O ₃ (0001) subs.	Twinned crystal	0.42	0.25	4.958	13.586	0.0991	0.293	2.2

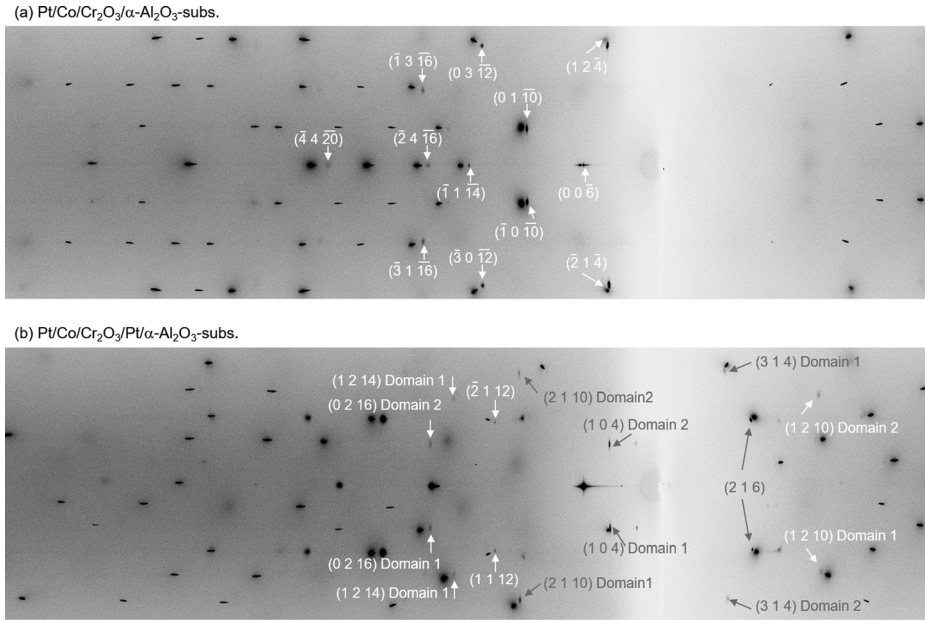


FIG. 4. Two-dimensional X-ray diffraction patterns of (a) α - Al_2O_3 (0001)-subs. and (b) Pt(111) buffer layer. The incident angle of X-ray is 10° – 15° . The black and gray arrows indicate the diffractions of the Cr_2O_3 layer. Here, the representative indexes are shown. Domains 1 and 2 denote the twin domains in which the $[100]$ of Cr_2O_3 is parallel and antiparallel to that of the α - Al_2O_3 substrate, respectively.

integrated intensity was corrected using the Lorentz factor (L), the polarization factor (P), and the absorption factor (A). The structural factor, $(F_{\text{hkl_exp}})^2 \propto I_{\text{exp}}/(L \cdot P \cdot A)$, was calculated for various $(h k l)$ peaks. The $(F_{\text{hkl_exp}})^2$ values were compared with the calculated structural factor, $(F_{\text{hkl_cal}})^2$, for various $(h k l)$ diffraction peaks, and ν and w were estimated by minimizing the standard deviation, σ , of $(F_{\text{hkl_exp}})^2/(F_{\text{hkl_cal}})^2$. As a typical result, $(F_{\text{hkl_exp}})^2/(F_{\text{hkl_cal}})^2$ values for various $(h k l)$ calculated for various w values for the film on the α - Al_2O_3 substrate are shown in Fig. 6(a). Note that since the $(h k l)$ diffractions used in Fig. 6(a) are insensitive to ν , i.e., the O^{2-} position, ν was fixed at a bulk value of $\nu = 0.3060$. From the change in σ with w [Fig. 6(b)], we estimated $w = 0.0963$ for the film on the α - Al_2O_3 substrate.

Since the diffraction peaks shown in Fig. 6(a) are insensitive to ν , we further measured the one-dimensional $2\theta/\omega$ profiles for the ν -sensitive diffractions: $(\bar{3}21)$ and $(7\bar{2}3)$. In Fig. 6(c), the change in $(F_{\text{hkl_exp}})^2/(F_{\text{hkl_cal}})^2$ for the two

peaks with ν is shown for the film on the α - Al_2O_3 (001) substrate. $(F_{\text{hkl_exp}})^2/(F_{\text{hkl_cal}})^2$ increases with ν for the $(\bar{3}21)$ diffraction but decreases with ν for the $(7\bar{2}3)$ diffraction. The intersection of the two curves gives the smallest σ , and ν is estimated as 0.322. In the same way, w and ν for the film on the Pt buffer layer are estimated as 0.0991 and 0.293, respectively.

Using the estimated lattice constants and the Cr^{3+} ion position, K_{dip} is calculated as

$$K_{\text{dip}} = E_{\mathbf{m}_1, \mathbf{m}_2 \parallel \langle 100 \rangle} - E_{\mathbf{m}_1, \mathbf{m}_2 \parallel \langle 001 \rangle}$$

$$E = \frac{1}{4\pi\mu_0 r^3} \left\{ (\mathbf{m}_1 \cdot \mathbf{m}_2) - \frac{3}{r^2} (\mathbf{m}_1 \cdot \mathbf{r})(\mathbf{m}_2 \cdot \mathbf{r}) \right\}, \quad (3)$$

where \mathbf{m}_1 and \mathbf{m}_2 are the spin vectors and \mathbf{r} is a position vector between the spin vectors. In the calculation, we assumed the magnetic moment of Cr^{3+} in the Cr_2O_3 layer as $2.48 \mu_B$.⁴⁴ $E_{\mathbf{m}_1, \mathbf{m}_2 \parallel \langle 100 \rangle}$ and $E_{\mathbf{m}_1, \mathbf{m}_2 \parallel \langle 001 \rangle}$ denote the energy where all the

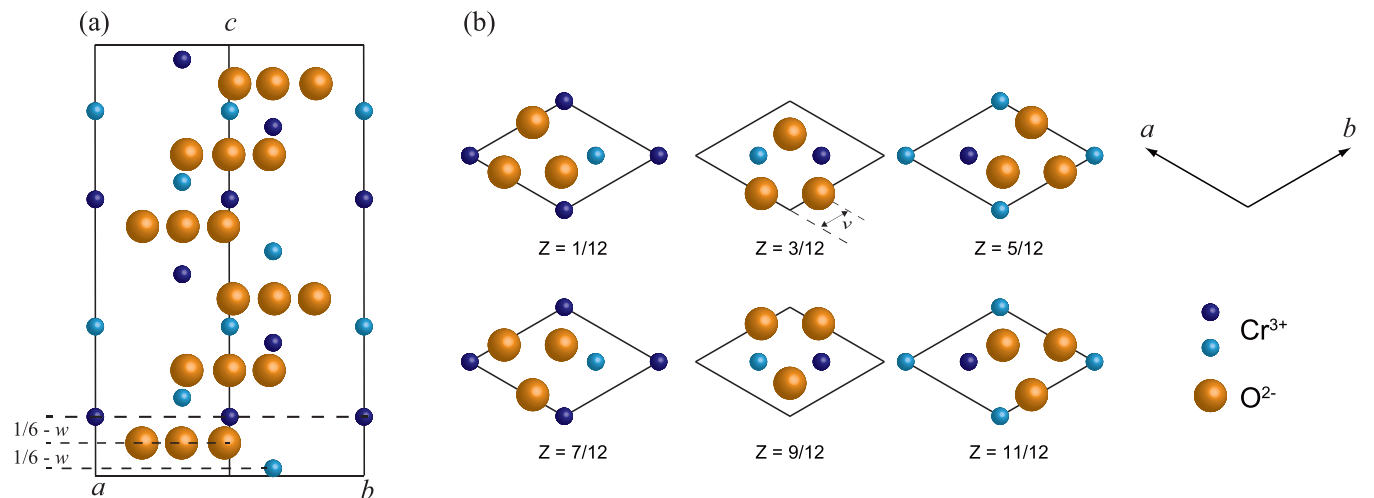


FIG. 5. Schematic drawing of the atom arrangement of each layer. The small and big circles represent the Cr^{3+} and O^{2-} ions, respectively. (a) $(11\bar{2}0)$ projection-view and (b) layer-resolved atom arrangements of each O^{2-} layer. The small thin and small thick circles represent the Cr^{3+} ions located slightly above ($Z - w + 1/6$) and below ($Z + w - 1/6$) the z -position of the O^{2-} lattice (Z), respectively.

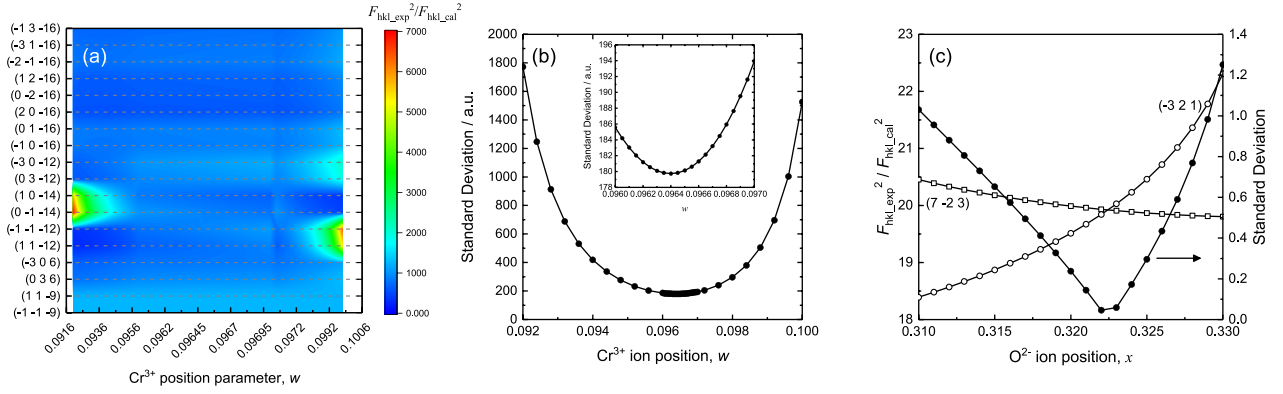


FIG. 6. (a) $F_{\text{hkl,exp}}^2 / F_{\text{hkl,cal}}^2$ for various (hkl) diffractions and (b) change in standard deviation as a function of the Cr^{3+} position parameter w . (c) $F_{\text{hkl,exp}}^2 / F_{\text{hkl,cal}}^2$ for (723) and (321) diffractions and standard deviation as a function of the O^{2-} position parameter v . The results shown are for the $\text{Pt/Co/Cr}_2\text{O}_3/\alpha\text{-Al}_2\text{O}_3$ -substrate.

spin vectors are along the a axis and c axis, respectively. In this definition, a positive K_{dip} represents perpendicular magnetic anisotropy. Since there are 12 Cr^{3+} ions in a unit cell, 12 spin-pairs per Cr^{3+} ion can be considered per unit cell. In this study, we expanded 15 unit cells in $\pm x$, $\pm y$, and $\pm z$ directions. Namely, in the 31^3 unit cells, the ΔE values for $31^3 \times 12 = 357\,491$ spin pairs are averaged. The calculated K_{dip} for the two films is shown in Fig. 7, and the K_{dip} calculated using the bulk parameters and the change in K_{dip} as a function of w proposed by Artman *et al.*^{27,45} are shown for comparison. K_{dip} is enhanced for the film on the Pt buffer layer, and suppressed to almost 0 for the film on the $\alpha\text{-Al}_2\text{O}_3$ substrate. It is likely that the change in K_{dip} agrees with that in K_{K} for the two films. The O^{2-} position parameter affects K_{FS} through the crystal field at the Cr^{3+} position although it is not considered in the estimation of K_{dip} . Although at the present state, it is difficult to estimate K_{FS} quantitatively, we present the qualitative discussion as follows. K_{FS} can be expressed by $-S(S-1/2)D$ ^{27,46} (where S is the spin quantum number and $2D$ represents the ground state splitting), and the crystal field from the O^{2-} lattice induce the ground state splitting ($2D$). Although both point

charge and electric dipolar moment contribute to the crystal field, the contribution of point charge is significant on D .^{47,48} Hence, assuming the point charge model here,⁴⁸ we estimated the strength of the exchange splitting, Dq , by the crystal field on the Cr^{3+} site using the obtained crystal parameters for the two types of films. For the calculation, we considered six nearest-neighboring O^{2-} ions. Dq can be expressed by using the crystal field components B_4^0 and B_4^3 as follows:

$$Dq = \left\{ \frac{3\sqrt{2}}{4} B_4^3 - \frac{4}{27} \left[B_4^0 + \frac{B_4^3}{20\sqrt{2}} \right] \right\} \frac{2}{105} \langle r^4 \rangle$$

$$B_4^0 = \frac{e}{64R^5} (35 \cos^4 \theta - 30 \cos^2 \theta + 3)$$

$$B_4^3 = \frac{70e}{16R^5} \sin^3 \theta \cos \theta \cos 3\phi. \quad (4)$$

Here, $\langle r^4 \rangle$ represents the expectation value of r^4 of an electron, R , θ , and ϕ are the coordinates of a lattice site, and the quantity e was given the value 14.3923 eV. We followed the above definitions and the unit of B_4^0 and B_4^3 given in reference 47. In Table II, the calculated Dq in terms of $\langle r^4 \rangle$, B_4^0 , and B_4^3 is shown. Dq becomes smaller for the film on the Pt buffer layer than for the film on the $\alpha\text{-Al}_2\text{O}_3$ substrate. Since K_{FS} is opposite in sign to D , the decrease in Dq implies an increase in $K_{\text{AFM}} (=K_{\text{dip}} + K_{\text{FS}})$. However, concurrently, the change in the crystal parameter can alter the electron density of Cr^{3+} ions via the change in volume of the O^{2-} octahedron lattice, V_{OCT} . As listed in Table II, the calculated V_{OCT} of the film on the Pt buffer layer is lower than that of the film on the $\alpha\text{-Al}_2\text{O}_3$ substrate. The small V_{OCT} would decrease the magnetic moment of Cr^{3+} as expected from the analogy of the magneto-volume effect. That is, K_{FS} can either increase or decrease depending on the variation in Dq and magnetic moment. For the quantitative estimation of K_{FS} , a first principles calculation is required, which is a nontrivial problem. The difficulty is partly because the absolute value of K_{AFM} of Cr_2O_3 is small ($2 \times 10^4 \text{ J/m}^3$),⁴⁹ which is near the typical accuracy of calculation, and future work is expected. The O^{2-} position parameter reflects the degree of asymmetry of the O^{2-} sub-lattice; the O^{2-} triangle size is asymmetric above and below the Cr^{3+} ion (see Fig. 5), and at $v = 0.333$, this asymmetry vanishes. The asymmetry of the O^{2-} triangle above and below the Cr^{3+}

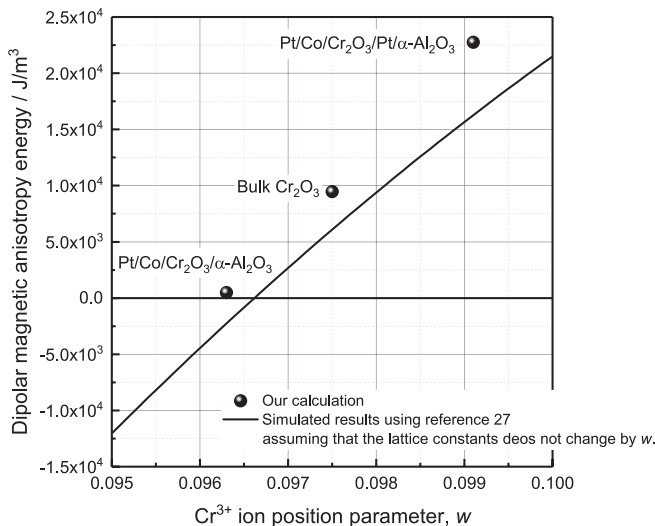


FIG. 7. Calculated perpendicular magnetic anisotropy energy density (K_{dip}) for the fabricated film. The calculated K_{dip} for bulk Cr_2O_3 and the simulated curve (solid line) proposed in Ref. 27 are also shown.

TABLE II. Calculated Dq , B_4^0 , B_4^3 at the Cr^{3+} site from the nearest neighbor O^{2-} octahedron lattice based the point charge model⁴⁸ and volume of O^{2-} octahedron lattice V_{OCT} . The unit of B_4^0 , B_4^3 are same as Ref. 48.

Underlayer/substrate	Dq	B_4^0	B_4^3	V_{OCT} (\AA^3)
$\alpha\text{-Al}_2\text{O}_3(0001)$ subs.	$0.0756\langle r^4 \rangle$	-0.117	3.744	11.80
Pt(111) buffer layer/ $\alpha\text{-Al}_2\text{O}_3(0001)$ subs.	$0.0716\langle r^4 \rangle$	-0.115	3.547	11.39

originates from the magneto-electric (ME) effect of Cr_2O_3 .^{50,51} A comparison of our results (Table I) with the bulk value revealed that the asymmetry of the O^{2-} lattice is enhanced on the Pt buffer layer and may yield a high ME coefficient. The direct estimation of the ME coefficient is currently the subject of a future study.

IV. SUMMARY

We fabricated two types of Pt/Co/ Cr_2O_3 films onto different underlayers, yielding differences in the in-plane crystalline quality and exchange anisotropy energy density. When the film is grown on $\alpha\text{-Al}_2\text{O}_3(0001)$, the Cr_2O_3 layer is single crystalline and the exchange anisotropy energy is 0.098 mJ/m^2 . In contrast, the film grown on Pt(111)-buffered $\alpha\text{-Al}_2\text{O}_3(0001)$ is twinned and exhibits a high exchange anisotropy energy of 0.42 mJ/m^2 . We investigated the difference in the exchange anisotropy energy density based on the specific ion positions of Cr^{3+} and O^{2-} in the Cr_2O_3 layer by analyzing the X-ray diffraction intensities. Using the estimated structural parameters, we calculated the magnetic anisotropy energy of Cr_2O_3 originating from the dipolar interaction between Cr^{3+} ions. The dipolar interaction energy is approximately 70 times higher for the film on the Pt buffer layer than that for the film on the $\alpha\text{-Al}_2\text{O}_3$ substrate, and the tendency roughly agrees with the change in the exchange anisotropy energy density.

ACKNOWLEDGMENTS

Y.S. thanks Dr. Chiharu Mitsumata of NIMS and Dr. Hiroshi Imamura and Dr. Yukie Kitaoka of AIST for their valuable discussions. The synchrotron experiments were carried out with the approval of KEK as a proposal (Grant No. 2013V001). This work was partly supported by JSPS KAKENHI (Grant Nos. 16H03832 and 16H02389), the ImPACT program of the Council for Science, Technology, and Innovation (Cabinet Office, Government of Japan), and the Izumi Scientific Foundation.

¹W. H. Meiklejohn and C. P. Bean, *Phys. Rev.* **102**, 1413 (1956).

²J. Nogués and I. K. Schuller, *J. Magn. Magn. Mater.* **192**, 203 (1999).

³A. E. Berkowitz and K. Takano, *J. Magn. Magn. Mater.* **200**, 552 (1999).

⁴R. L. Stamps, *J. Phys. D: Appl. Phys.* **33**, R247 (2000).

⁵B. Dieny, V. S. Sperioum, S. Metin, S. S. P. Parlin, B. A. Gurney, P. Baumgart, and D. R. Wilhoit, *J. Appl. Phys.* **69**, 4774 (1991).

⁶S. Ikeda, J. Hayakawa, Y. M. Lee, F. Matsukuram, Y. Ohno, T. Hanyu, and H. Ohno, *IEEE Trans. Electron Devices* **54**, 991 (2007).

⁷K. Imakita, M. Tsunoda, and M. Takahashi, *Appl. Phys. Lett.* **85**, 3812 (2004).

⁸Y. F. Liu, J. W. Cai, and S. L. He, *J. Phys. D: Appl. Phys.* **42**, 115002 (2009).

⁹H. Takahashi, M. Tsunoda, and M. Takahashi, *IEEE Trans. Magn.* **48**, 4347 (2012).

¹⁰Y. Shiratsuchi, T. Fujita, H. Oikawa, H. Nnoutomi, and R. Nakatani, *Appl. Phys. Express* **3**, 113001 (2010).

¹¹Y. Shiratsuchi, W. Kuroda, T. V. A. Nguyen, Y. Kotani, K. Toyoki, T. Nakamura, M. Suzuki, K. Nakamura, and R. Nakatani, *J. Appl. Phys.* **121**, 073902 (2017).

¹²Y. Shiratsuchi, K. Wakatsu, T. Nakamura, H. Oikawa, S. Manou, Y. Narumi, K. Tazoe, C. Mitsumata, T. Kinoshita, H. Nojiri, and R. Nakatani, *Appl. Phys. Lett.* **100**, 262413 (2012).

¹³P. Borisov, A. Hochstrat, X. Chen, W. Kleemann, and C. Binek, *Phys. Rev. Lett.* **94**, 117203 (2005).

¹⁴Y.-H. Chu, L. W. Martin, M. B. Holcomb, M. Gajek, S.-J. Han, Q. He, N. Balke, C.-H. Yang, D. Lee, W. Hu, Q. Zhan, P.-L. Yang, A. Fraile-Rodriguez, A. Scholl, S. X. Wang, and R. Ramesh, *Nat. Mater.* **7**, 478 (2008).

¹⁵X. He, Y. Wang, N. Wu, A. N. Caruso, E. Voscovo, K. D. Belashchenko, P. A. Dowben, and C. Binek, *Nat. Mater.* **9**, 579 (2010).

¹⁶K. Toyoki, Y. Shiratsuchi, A. Kobane, C. Mitsumata, Y. Kotani, T. Nakamura, and R. Nakatani, *Appl. Phys. Lett.* **106**, 162404 (2015).

¹⁷T. Ashida, M. Oida, N. Shimomura, T. Nozaki, T. Shibata, and M. Sahashi, *Appl. Phys. Lett.* **106**, 132407 (2015).

¹⁸Y. Shiratsuchi and R. Nakatani, *Mater. Trans.* **57**, 781 (2016).

¹⁹T. V. A. Nguyen, Y. Shiratsuchi, and R. Nakatani, *Appl. Phys. Express* **10**, 083002 (2017).

²⁰T. V. A. Nguyen, Y. Shiratsuchi, A. Kobane, S. Yoshida, and R. Nakatani, *J. Appl. Phys.* **122**, 073905 (2017).

²¹A. P. Malozemoff, *Phys. Rev. B* **35**, 3679 (1987).

²²A. P. Malozemoff, *Phys. Rev. B* **37**, 6903 (1988).

²³A. P. Malozemoff, *J. Appl. Phys.* **63**, 3874 (1988).

²⁴D. Mauri, H. C. Siegmann, P. S. Bagus, and E. Kay, *J. Appl. Phys.* **62**, 3047 (1987).

²⁵N. C. Koon, *Phys. Rev. Lett.* **78**, 4865 (1997).

²⁶M. Tachiki and T. Nagamiya, *J. Phys. Soc. Jpn.* **13**, 452 (1958).

²⁷J. O. Artman, J. C. Murphy, and S. Foner, *Phys. Rev.* **138**, A912 (1965).

²⁸Y. Shiratsuchi, H. Noutomi, H. Oikawa, T. Nakamura, M. Suzuki, T. Fujita, K. Arakawa, Y. Takechi, H. Mori, T. Kinoshita, M. Yamamoto, and R. Nakatani, *Phys. Rev. Lett.* **109**, 077202 (2012).

²⁹K. Toyoki, Y. Shiratsuchi, T. Nakamura, C. Mitsumata, S. Harimoto, Y. Takechi, T. Nishimura, H. Nomura, and R. Nakatani, *Appl. Phys. Express* **7**, 114201 (2014).

³⁰M. Tsunoda, H. Takahashi, T. Nakamura, C. Mitsumata, S. Isogami, and M. Takahashi, *Appl. Phys. Lett.* **97**, 072501 (2010).

³¹H. Takahashi, Y. Kota, M. Tsunoda, T. Nakamura, K. Kodama, A. Sakuma, and M. Takahashi, *J. Appl. Phys.* **110**, 123920 (2011).

³²C. Mitsumata, M. Tsunoda, H. Takahashi, and A. Sakuma, *Europhys. Lett.* **99**, 47006 (2012).

³³K. D. Belashchenko, *Phys. Rev. Lett.* **105**, 147204 (2010).

³⁴M. Suzuki, H. Muraoka, Y. Inaba, H. Miyayama, N. Kawamura, T. Shimatsu, H. Maruyama, N. Ishimatsu, Y. Isohama, and Y. Sonobe, *Phys. Rev. B* **72**, 054430 (2005).

³⁵Y. Shiratsuchi, T. Fujita, H. Noutomi, H. Oikawa, and R. Nakatani, *IEEE Trans. Magn.* **47**, 3909 (2011).

³⁶International Tables for Crystallography vol. C, 2nd ed., Table 6.1.1.4.

³⁷S. Sasaki, KEK Report 88-14, 1, 1989.

³⁸J. H. Underwood and T. W. Babee, Jr., *Appl. Opt.* **20**, 3027 (1981).

³⁹T. Shinjo and T. Takada, *Metallic Superlattices* (Elsevier, Netherlands, 1987), pp. 65–67.

⁴⁰A. Stierle, T. Koll, and H. Zabel, *Phys. Rev. B* **58**, 5062 (1998).

⁴¹Landolt-Börnstein, *New Series, Group III* (Springer-Verlag, Berlin, 1975), Vol. 7, p. 242.

⁴²International Tables for X-Ray Crystallography (Kynoch Press, 1967), Vol. 3..

⁴³E. Hovestreydt, *Acta Crystallogr., Sect. A* **39**, 268 (1983).

⁴⁴P. J. Brown, J. B. Forsyth, E. Lelièvre-Berna, and F. Tasset, *J. Phys.: Condens. Matter* **14**, 1957 (2002).

⁴⁵Our calculated K_{dip} is higher than that by Artman *et al.*, because their simulation underestimates K_{dip} because of the insufficient calculation range, a sphere with the diameter of $6a$ caused by the limitation of the computer at the time.

⁴⁶K. Yoshida, *Prog. Theor. Phys.* **6**, 691 (1951).

⁴⁷R. R. Sharma and T. P. Das, *J. Chem. Phys.* **41**, 3581 (1964).

⁴⁸D. S. McClure, *J. Chem. Phys.* **36**, 2757 (1962).

⁴⁹S. Foner, *Phys. Rev.* **130**, 182 (1963).

⁵⁰R. M. Hornreich and S. Shtrikman, *Phys. Rev.* **161**, 506 (1967).

⁵¹M. Fiebig, *J. Phys. D: Appl. Phys.* **38**, R123 (2005).